applied optics

Dynamic point shifting with null screens using three LCDs as targets for corneal topography

M. I. Rodríguez-Rodríguez,[1,2,*] A. Jaramillo-Núñez,[1] and R. Díaz-Uribe[2]

[1]Instituto Nacional de Astrofísica, Óptica y Electrónica, Apdo. Postal No. 51, Puebla, Pue. 72000, Mexico
[2]Universidad Nacional Autónoma de México, Centro de Ciencias Aplicadas y Desarrollo Tecnológico, Apdo. Postal No. 70-186, C. P. 04510, México D. F., Mexico
*Corresponding author: martin.rodriguez@ccadet.unam.mx

Received 16 March 2015; revised 20 May 2015; accepted 24 June 2015; posted 24 June 2015 (Doc. ID 236222); published 24 July 2015

In this paper, the use of three liquid crystal displays (LCDs) as targets for an experimental corneal topographer is proposed. The main advantage is that the geometrical pattern in the target can be modified without moving any mechanical part to apply the dynamic point shifting (DyPoS) method. Some results on the capabilities of the LCDs, obtained with photo frames, for measuring a 6.37 mm radius of curvature calibration sphere, and applying the DyPoS method, are presented. It is shown that the error in measuring the radius of curvature with DyPoS is reduced to 3% of the real value and the RMS in elevation or sagitta differences is around 15 μm, 30% or 66% of the values obtained without DyPoS, respectively.

OCIS codes: (170.3890) Medical optics instrumentation; (170.4460) Ophthalmic optics and devices; (120.6650) Surface measurements, figure; (120.4640) Optical instruments; (170.4580) Optical diagnostics for medicine.

http://dx.doi.org/10.1364/AO.54.006698

1. INTRODUCTION

In early works [1,2], a method for testing fast aspheric convex surfaces with a cylindrical null screen has been reported; in this method, the design screen is plotted on a sheet of paper with the help of a laser printer; then the paper is rolled into a cylindrical shape and inserted into a transparent acrylic cylinder that supports the paper. More recently, new techniques have been developed in order to quantitatively evaluate very fast aspheric surfaces with the null screen method [1–5]. In all cases, the essential idea consists of designing the screen with a set of spots in such a way that the image reflected by the test surface gives a perfectly ordered arrangement if the test surface is perfect; assuming that the ideal shape of the surface to evaluate (reference surface) is known, the position and shape of the spots on the screen can be easily computed. This technique has the advantage that it does not need any additional optical element with a specific design to correct the aberrations of the system under test. The test with screens has a great similarity with the Hartmann test [6], but it differs in several aspects; for instance, it does not require a point source or a screen with holes used to select rays. A common aspect of both testing methods and of all those methods that measure the slope of the wavefront is that the quantitative evaluation is made by means of a numerical integration process. An important problem with this procedure is that the integration method (for instance, the trapezoidal rule) accumulates errors throughout the integration path. It is well known that the larger the path, the greater the accumulated error. In addition, it is also well known that for the trapezoidal rule, the error increases as the second power of the spacing between the spots of the integration path [7]. Thus, to minimize error, it is desirable to reduce the spacing between spots. This implies more spots in the null screen; there exists, however, a physical limit, because if the spot density is too large, then the spot images can overlap because of defocus, aberrations, or, in the best case, by diffraction. This situation makes the evaluation of the centroids of the spots more difficult.

On the other hand, many commercially available topographers still use Placido's disk target in order to evaluate the human cornea, which consists of a set of circular, concentric rings on a flat surface; the target surface has evolved into a conical, hemispherical, cylindrical, or even ellipsoidal surface [8], with the aim of flattening the image surface. One possible limitation of Placido-based systems is the ambiguity of data in the azimuthal direction; this is known as the skew ray problem [9–14]. In addition, Joris Snellenburg *et al.* stated [15] that to solve the skew ray error problem of Placido-based systems, the approach used by some authors has been to use different target designs that allow one-to-one correspondence between image points and target points [16–18]; for these systems, it is possible to develop reconstruction algorithms that avoid skew ray errors [19–21]. For that reason, new generations of topographers that use targets with a set of separate spots located on an oval [8] or cylindrical screen [22], or by multicamera corneal topographer

arrangements using a thin-film-transistor (TFT) liquid-crystal display for displaying a measurement pattern [23], have been proposed recently; in the last case, however, the experimental image obtained is not a flat image, as is the case of the oval screen [8] or the cylindrical screen [22], with a good approximation. Other kinds of topographers could be created with LEDs on a cone [24], or even a checkerboard-type target also printed on a cone [12] has been proposed; they have the advantage over the classical targets in that they overcome the skew ray problem. In this way, each method has a static target that must be used for every measurement, no matter the size and shape of the cornea under study. Furthermore, it has been recognized that null screens with chromatic or colored spots [25,26] can be advantageous to evaluate highly deformed optical surfaces; this is the case of the cornea.

Following the proposal of Moreno-Oliva *et al.* [27], in this paper the use of liquid crystal displays (LCDs) as null screens for testing or measuring the shape, curvature, and dioptric power, among other quantities, of the anterior corneal surface is proposed; i.e., the classical static target of a corneal topographer is substituted by a set of LCDs. The proposed null screen is now displayed on LCD flat screens instead of the traditional cylindrical null screen [1,3]; the positions of the drop-shaped spots [28] can be programmed to be displayed in a dynamic way for performing the shifting of the spots. In this method, the design of the null screen is made by a similar procedure as that proposed in Ref. [27]; the appropriate equations used for this array, however, are shown in a preliminary fashion in Ref. [28]. As in Ref. [27], in this paper the dynamic point shifting method (DyPoS), without applying any mechanical movement, is used. Many configurations of LCDs can be used for the testing; in this paper, however, three LCDs forming a triangular prism as the target in an experimental corneal topographer to measure the shape of human corneas is described.

A first proposal of this method was made in 2011 [28]; here, the quantitative evaluation of a calibration sphere is reported. In Section 2, the optical setup and the corresponding equations for the design of the null screens for implementing DyPoS are developed. In Section 3, the test of a calibration sphere is fully explained; in Section 4, additional capabilities of this proposal are described. Finally, conclusions are listed in Section 5.

2. PROPOSED METHOD

In Ref. [27], an array of four flat screens was used to test a nearly parabolic convex surface, although three are enough for doing this task. The proposed setup consists of three LCDs placed in a triangular prism arrangement, which will be used in order to display the null-screen target, for evaluating a calibration sphere used to simulate the corneal surface. In this configuration, the eye is placed on one aperture, whereas the camera is placed on the opposite aperture. The focal length of the camera lens is selected in such a way that the image of the surface fits inside the CMOS sensor; furthermore, the test surface and the lens must be separated by at least a distance equal to the length of the LCD. For that reason, a 110 mm focal length telephoto lens was used. In Fig. 1, the basic setup is shown.

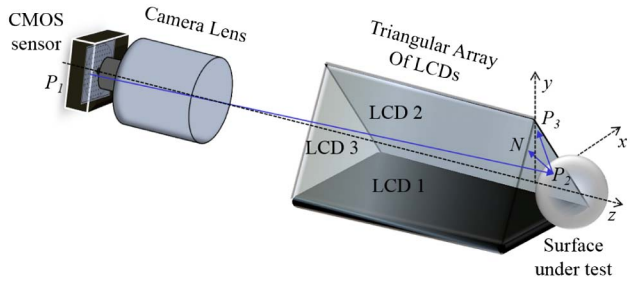

Fig. 1. Layout of the testing configuration.

A ray starting at $\boldsymbol{P}_3$ on the null screen reaches the image plane at $\boldsymbol{P}_1$, after being reflected by the surface (cornea) at $\boldsymbol{P}_2$. Additionally, an image-forming optical system must be used to project the virtual image, formed by reflection on the optical surface, on a CMOS sensor. Indeed, the optical system may introduce a small amount of distortion, but this can be taken into account by calibrating the system.

A. Calculation of Points on the Screen

The variables involved in the design of the flat null screen displayed on the LCD monitors are shown in Fig. 2; in addition, the cardinal points of the camera lens are shown. In this case, the thin-lens approximation used in other papers [1–5,8] is no longer used. The principal planes H_1 and H_2 are disposed in reversed order, because a telephoto lens is used; in the real direction of the ray propagation, H_2 is first encountered by a ray reflected on the test surface, but the ray must be propagated without deviation to nodal point N_1; then the ray goes back, parallel to the optical axis, to the other nodal point N_2; from this point, the ray is deviated again to find its final direction after the lens, parallel to the original incident ray.

To determine the points on the screen that produce a square array of spots in the image plane, a reverse exact ray-tracing calculation is performed, in a similar way to that developed for calculating cylindrical screens to test fast convex surfaces [1]; the final expressions are quite similar, but they differ in the use of a thick camera lens, as was explained above, and in the shape of the null-screen surface.

The point $\boldsymbol{P}_1 = (x_1, y_1, -a - b)$ are the Cartesian coordinates of a point on the CMOS sensor, where a is the distance between the second principal plane (H_2) and the CMOS sensor and b is the distance between the first principal plane (H_1) and the vertex (V) of the surface under test. A ray is traced back

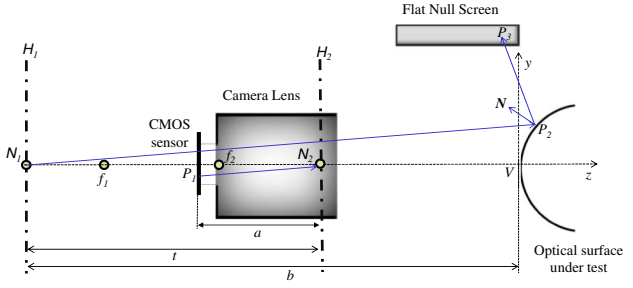

Fig. 2. Variables involved in the calculation of the flat null screen. The rays are drawn in the reverse direction for the design of the null screen.

from $\boldsymbol{P}_1$ to the CMOS sensor inversely as was explained above; this ray has a direction represented by the vector

$$\vec{I} = (\vec{N}_2 - \vec{P}_1) = (-x_1, -y_1, a). \tag{1}$$

The coordinates $\boldsymbol{P}_2 = (x_2, y_2, z_2)$ of the point of incidence on the surface are obtained by intersecting the incident ray and the test surface. The incident ray can be written as

$$\begin{aligned} x_2 &= -\sigma x_1, \\ y_2 &= -\sigma y_1, \\ z_2 &= -b + \sigma a, \end{aligned} \tag{2}$$

where σ is the parameter of the corresponding straight line equation. The test surface is unknown; in order to solve this, only for design purposes, an approximating analytical surface called a reference surface is used; a good choice is to use a conical surface such as

$$\phi(x_2, y_2, z_2) = (k+1)z_2^2 - 2z_2 r + x_2^2 + y_2^2, \tag{3}$$

where r is the radius of curvature at the vertex and k the conic constant; this surface has its vertex at the origin of coordinates. By substituting Eq. (2) in Eq. (3) and solving for σ, the correct value of the parameter to be used in Eq. (2) is obtained.

The reflected ray is calculated through the vector reflection law

$$\hat{R} = \hat{I} - 2(\hat{I} \cdot \hat{N})\hat{N} = (R_x, R_y, R_z), \tag{4}$$

where

$$\hat{I} = \frac{\vec{I}}{\|\vec{I}\|}, \tag{5}$$

is the unit incident vector and $\hat{N} = (n_x, n_y, n_z)$ is the unit vector normal to the reference surface at the incidence point P_2; $\hat{N}$ can be calculated as

$$\hat{N} = \frac{\nabla\phi(x_2, y_2, z_2)}{|\nabla\phi(x_2, y_2, z_2)|}. \tag{6}$$

Then, by substituting Eqs. (1), (3), (5), and (6) in Eq. (4), the components of the reflected ray are obtained as

$$\begin{aligned} R_x &= -x_1 - 2x_2 \frac{\{-x_1x_2 - y_1y_2 + a[(k+1)z_2 - r]\}}{x_2^2 + y_2^2 + [(k+1)z_2 - r]^2}, \\ R_y &= -y_1 - 2y_2 \frac{\{-x_1x_2 - y_1y_2 + a[(k+1)z_2 - r]\}}{x_2^2 + y_2^2 + [(k+1)z_2 - r]^2}, \\ R_z &= a - 2[(k+1)z_2 - r] \frac{\{-x_1x_2 - y_1y_2 + a[(k+1)z_2 - r]\}}{x_2^2 + y_2^2 + [(k+1)z_2 - r]^2}. \end{aligned} \tag{7}$$

Finally, the ray hits the corresponding flat null screen (LCD) at $\boldsymbol{P}_3 = (x_3, y_3, z_3)$. For this, every flat screen is defined by

$$y_3 = m_p x_3 + \beta_p, \tag{8}$$

where m_p is the slope of the straight line [see Fig. 3(a)] and the subscript $p = 1$, 2, and 3 accounts for each screen; β_p is the height where the plane intersects the y axis as indicated in Fig. 3(a). Correct values for m_p and β_p, for every LCD are listed in Table 1.

S_1 is the minimum distance from each LCD to the optical axis and c is the distance from the same axis to each of the edges

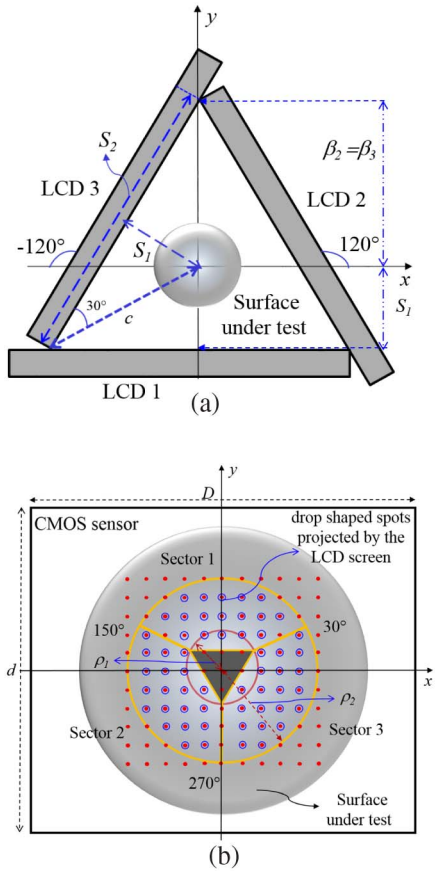

Fig. 3. (a) Transverse layout of the testing configuration. (b) Schematic diagram of the spots on the image plane (there is an additional image inversion due to the camera lens).

of the triangular LCD array; from Fig. 3(a), it is easy to find that

$$S_1 = \frac{S_2}{2} \tan(30°), \tag{9}$$

where S_2 is the width of one LCD screen.

In order to obtain the coordinates at the point $\boldsymbol{P}_3$, the reflected ray is described by the equation

$$\vec{P}_3 = \vec{P}_2 + \tau\vec{R}. \tag{10}$$

Intersecting this ray with each flat screen, the proper value of τ for each point on the target is found:

$$\tau = \frac{m_p x_3 + \beta_p - y_2}{R_y}, \tag{11}$$

Finally, by substituting Eq. (11) in Eq. (10), the corresponding coordinates of point $\boldsymbol{P}_3$ are obtained; they indicate where a

Table 1. Parameters for Describing the Three Flat Screens

p	m_p	β_p
1	0	$-S_1$
2	$\tan(2\pi/3) = -1.732$	c
3	$\tan(-2\pi/3) = \tan(\pi/3) = +1.732$	c

point P_3 must be placed on the LCD screen to see its image at point P_1 on the CMOS sensor image.

B. Design of Dots in the Image Plane

The null screen is designed in such a way that the CMOS sensor detects a square array of $(2M+1)^2$ spots with center coordinates given by

$$\left.\begin{aligned} x_{1u} &= ul \\ y_{1v} &= vl \end{aligned}\right\} u, v = 0, \quad \pm 1, \pm 2, \ldots, \pm M. \tag{12}$$

Indeed, Fig. 3(b) schematically represents these centers as a square array of red dots at the image plane on the CMOS sensor; this figure shows a possible design represented by Eq. (12), with $M = 5$. During the screen design, however, for some red dots, the reflected ray does not intersect some LCD; this is the case for the dots near the corners or the center of the square array. The only part of the image plane that is covered by the image of the dots is the region contained within a circle of radius ρ_2 and the central equilateral triangle; the circle is the image of the edges of the LCD near the surface, parallel to the (x, y) plane, whereas the triangle is the image of the far edges of the LCD. By considering an imaginary circle of radius ρ_1 that contains the triangle, the limits to the radial coordinates of the evaluation area on the image plane can be expressed as

$$\rho_1 < \sqrt{x_1^2 + y_1^2} < \rho_2. \tag{13}$$

Thus, the real number of dots is reduced accordingly; the red dots surrounded by the blue circles in Fig. 3(b) correspond to the dots observed in the image plane; the others are missing. The image of the LCD edges, parallel to the z axis, are straight lines at 30°, 150°, and 270°, which are shown as dark yellow straight lines in Fig. 3(b). Each LCD covers a sector making a 120° angle on the image; in Table 2, a detailed definition of the sectors is listed.

The total number of dots observed at the image is around

$$T = \text{floor}\left[\pi M^2 \left(1 - \frac{\rho_1^2}{\rho_2^2}\right)\right], \tag{14}$$

where function floor means the maximum integer less or equal to the argument.

On the other hand, it is well known that for a quantitative evaluation of the test surface [2–5], the experimental positions of the dots are obtained from the centroids of circular spots of the same diameter in the image plane. Then, each of the corresponding spots in the null screen must be designed in such a way that its image obtained by reflection on the reference surface gives a circle with center in the corresponding dot described above [Fig. 3(b)]. According to Heikkila [29], there are many factors that determine the accuracy of the evaluation of the spot centroid; with a proper treatment and analysis of the image spots, a subpixel accuracy of the order of 1/50 pixels can be attained. For the setup proposed in this paper, the relationship between the total number of pixels N_s contained in one spot and the standard deviation σ_c of the centroid coordinates for the same spot, after 10 different trials, is given by

$$\sigma_c = \frac{16.911}{N_s} + 0.0022. \tag{15}$$

Then for circular spots 10 pixels in diameter, $N_s = 78$ and $\sigma_c = 0.21$; assuming that σ_c is a good measure of the accuracy of the centroid evaluation, it is possible to get a subpixel accuracy of $1/\sigma_c = 1/4.6$ pixels. For a CMOS sensor with a pixel size of 3.6 μm, the accuracy of the centroid determination is 0.78 μm.

As for other null screens with different geometries (cylindrical [3–5], flat inclined [30,31], and cones [32]), the spots in the null-screen target have an almost elliptical shape; their size and orientation depend on the positon in the null screen; a schematic representation is shown in Fig. 3(b).

Table 2. Parameters for the Sectors on the Image Plane (see Fig. 3)[a]

Sector	$\mu_{\min}$(°)	$\mu_{\max}$(°)	x_1	y_1
1	tan (30)	tan (150)	$x_1 > \frac{y_1}{\mu_{\max}}$ for $x_1<0$; $x_1 < \frac{y_1}{\mu_{\min}}$ for $x_1>0$	$y_1 > 0$
2	tan (150)	tan (270)	$x_1 < 0$	$y_1 < \mu_{\max} x_1$
3	tan (270)	tan (390)	$x_1 > 0$	$y_1 > \mu_{\min} x_1$

[a]For all cases, $\rho_1 < \rho < \rho_2$ and $\rho_1 < |x_1| < \rho_2$.

C. DyPoS Method

The DyPoS method consists of changing the position of the spots on the null screen several times and getting a picture for each position; this increases the density of the evaluation points on the surface to be measured, increasing accordingly the lateral resolution of the measurement and reducing the truncation errors of the numerical integration procedure. To avoid mechanical movements of some part of the setup, a different image is displayed at every LCD of the target; each image shows a set of spots displaced with reference to any other image and each time a different spot image reflected off the surface is captured by the CMOS sensor. According to Refs. [3,4,27], the truncation error for the trapezoidal integration method is reduced to ε/η, where ε is the truncation error for a single image evaluation and η is the number of shifts (and captured images) of the spots.

For the point shifting, a different null screen must be designed; this is done as explained before, but the center of each spot in the CMOS sensor image must be located at

$$x_{u,i} = \left(u + \frac{i}{\eta}\right) l, \tag{16}$$

$$y_{v,j} = \left(v + \frac{j}{\eta}\right) l, \tag{17}$$

where $u, v = 0, \pm 1, \pm 2, \pm 3, \ldots, \pm M$ and $i, j = 0, 1, 2, \ldots, \eta - 1$; $l = d/(2M)$ is the separation between two adjacent spots and l/η is the distance shifted, along the x or y direction. The number of shifts performed on the screen and the number of images captured is η^2; the counters i and j are responsible for the dot shift. Figure 4(a) shows the point shifting method in the plane of the CMOS sensor, whereas in Fig. 4(b) the corresponding spot movements on each of the LCDs are shown. In both cases, the bright red spots are for no shift ($i = j = 0$); the green spots are for $i = 1$,

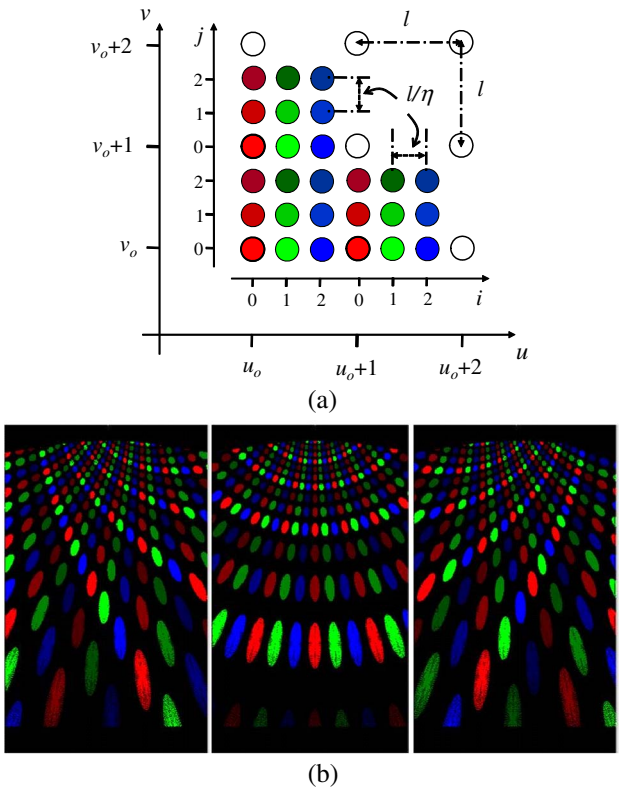

Fig. 4. (a) Schematic representation of DyPoS for $\eta = 3$. (b) Sequence of flat null screens displayed on LCD1, LCD2, and LCD3 monitors, by the DyPoS method.

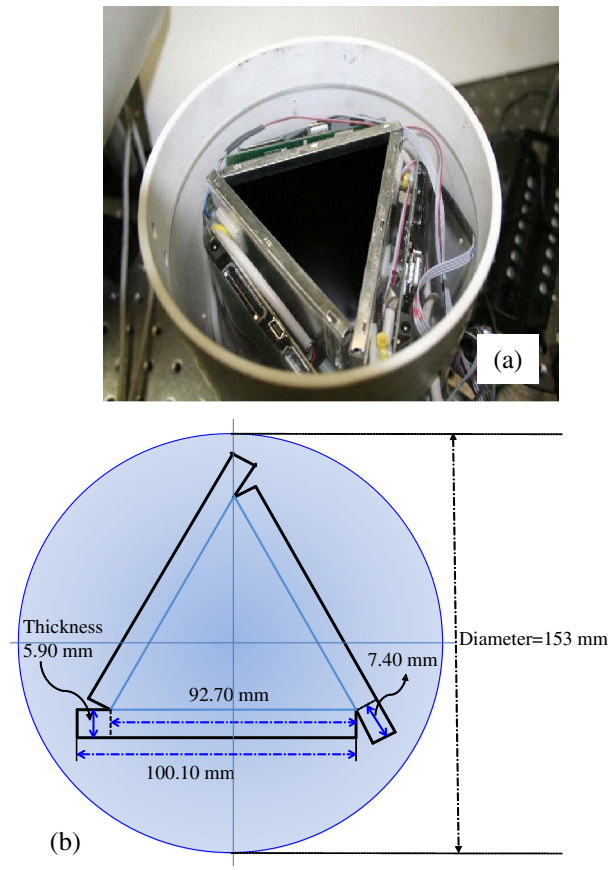

Fig. 5. (a) Triangular prism setup within a cylinder. (b) Profile of the laser cut on the lateral covers of the cylinder.

whereas the blue spots correspond to $i = 2$. The brightness of the spots is reduced with increasing j; the brightest spots are for $j = 0$ and the darker are for $j = 2$. The screens are designed for $M = 20$ and $\eta = 3$, giving a total of nine shifts (including the no shift).

3. EXPERIMENTAL SETUP

To demonstrate the feasibility of the proposed device and method, an experimental test is next described.

For the null screen target, we have used three identical standalone digital picture frames (DPFs), 7" DYNEX model DX-DPF7-10-MX. They are able to display only still pictures with resolution of 480 x 274 pixels (328 μm by side); their dimensions are 157 mm × 90 mm of active display area. The files of the images to be displayed are transferred to the internal DPF memory by means of a memory card or a USB flash memory; they cannot communicate directly with a computer. The DPF case was removed and the electronics were relocated to allow screens to be side by side to form the triangular prism, as shown in Fig. 5(a); the prism was inserted within a plastic cylindrical enclosure with a circular clear acrylic cover on each lateral opening. To ensure better alignment of the DPFs, on each cover the triangular profile of the prism was cut with laser as shown in Fig. 5(b).

Each null screen designed is displayed on the corresponding monitor. The test surface is a calibration sphere that is placed in front of the LCD array, along the symmetry or optical axis. The images are captured with a CMOS sensor ThorLabs model DCC1645C (1280 × 1027 pixels), together with a zoom lens system of focal length 110 mm. The setup and image obtained with it are shown in Fig. 6. The parameters used for the design of the null screen target are listed in Table 3.

The alignment of the surface was performed by using an overlay with a circle and a cross hair; the circular image of the boundary of the surface must be centered at the CMOS sensor. When this condition is fulfilled, the array of dots must be square, otherwise the target is misaligned or the testing surface is different from the design surface.

A. DyPoS Images

With the experimental setup shown in Fig. 6(a), DyPoS is applied. In Fig. 7, the original image [Fig. 6(b)] together with eight different images obtained for the same number of shifts are shown; to appreciate the details, the images are cut to show only the area where the spots are. In each of these images, a square arrangement of spots is formed.

From these separate images, it is not so easy to observe the shifts; so in Fig. 8, all the shifted spots are shown at one time. These images were created after processing the nine images in Fig. 7 and superimposing all the spots on the same image. Figure 8(a) shows all the spots in black, whereas the background is white as in the original images, but with improved contrast. For a better understanding, in Fig. 8(b) the spots are

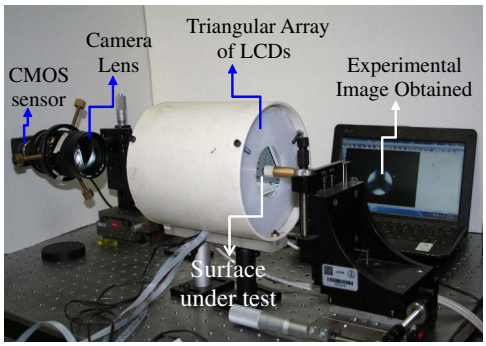

(a)

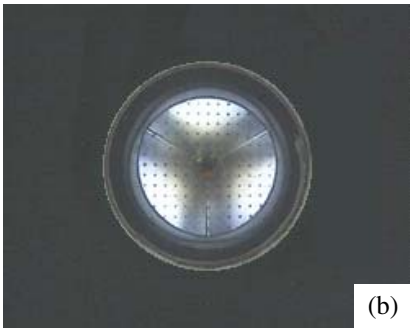

(b)

Fig. 6. (a) Experimental setup of three LCD screens forming a triangular prism. (b) Experimental image obtained.

colored so it is easier to identify each one and associate it with the applied shift; the color coding is the same as in Fig. 4 and is explained in the caption of Fig. 8.

B. Surface Shape Evaluation

Quantitative evaluation of the surface is performed by following the same procedure as in previous works [3–5,27,30–33]. First of all, each image is independently processed to calculate the centroid coordinates of every spot. To separate the spots pixels, an algorithm for smoothing the background was developed; this uses an image of the background illumination when there are no spots displayed (see Fig. 9). Then a simple thresholding method is used. The spot centroid coordinates are computed using the mass center formula, but using the intensity or gray level instead, as follows:

Table 3. Setup Parameters Used for the Design of the LCD Null Screen

Element	Parameter	Symbol	Size
Reference surface	Radius of curvature	r	6.37 mm
	Conic constant	k	0
Camera lens	First principal plane–vertex distance ($H_{1\text{-}V}$)	b	781.68 mm
	Second principal plane–CMOS distance (H_2–CMOS)	a	144 mm
Image sensor	Minimum length	d	3.6 mm
	Optical axis LCD distance	S_1	26.55 mm

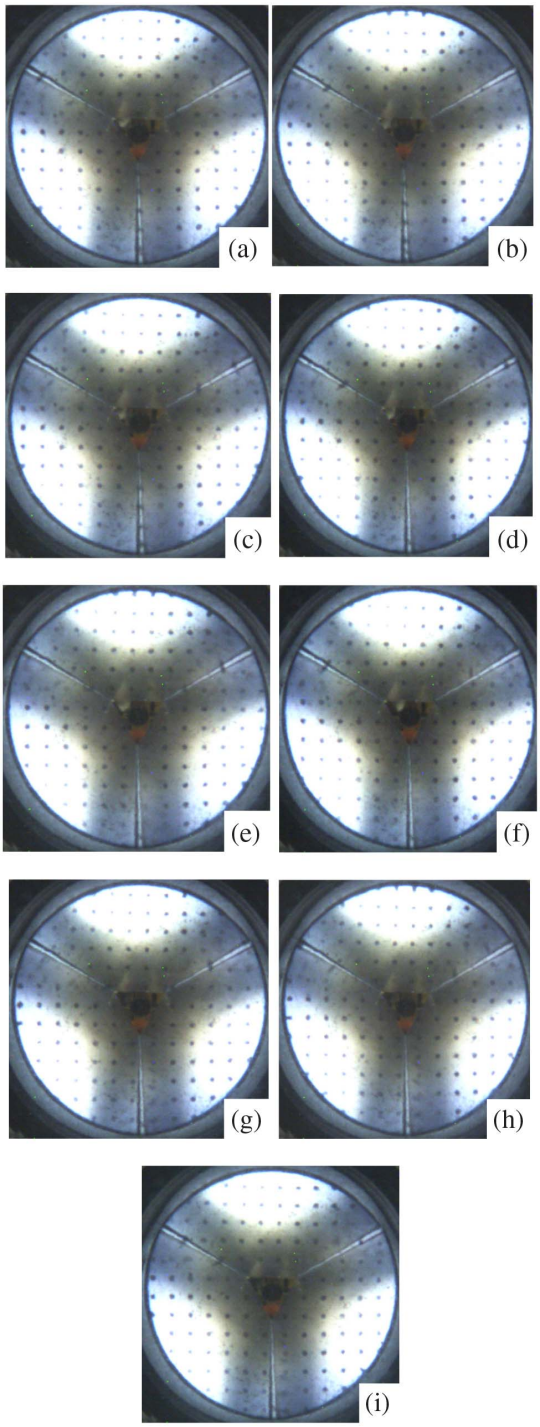

Fig. 7. Evolution of the image spots on the test surface, by the point shifting method for (i, j) given by (a) (0,0), (b) (0,1), (c) (0,2), (d) (1,0), (e) (1,1), (f) (1,2), (g) (2,0), (h) (2,1), and (i) (2,2).

$$\vec{r}_{ct} = \frac{\sum_{i=1}^{N_t} \vec{r}_{it} I_{it}}{\sum_{i=1}^{N_s} I_{it}}, \tag{18}$$

where $\vec{r}_{ct} = (x_{ct}, y_{ct})$ is the vector representing the centroid position of the tth spot on the sensor ($t = 1, 2, \ldots, T$), $\vec{r}_{it} = (x_{it}, y_{it})$ is the position vector of the ith pixel that belongs

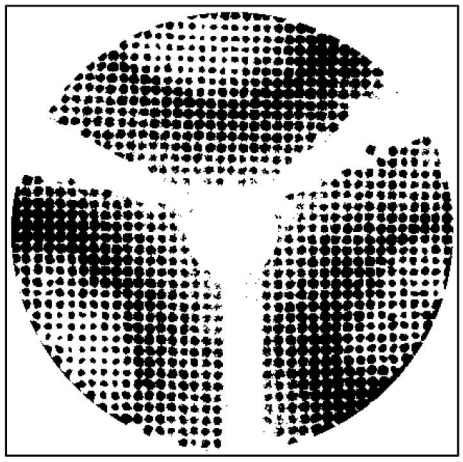

(a)

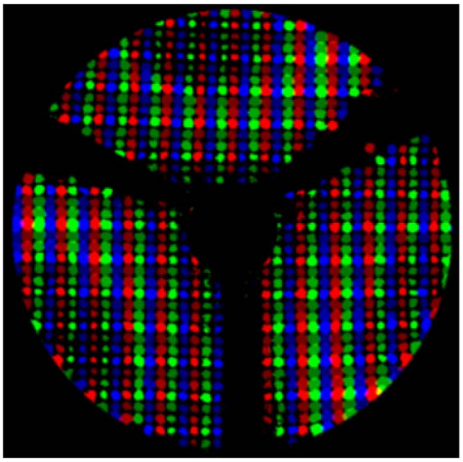

(b)

Fig. 8. Evolution of the image spots on the image of the test surface; these images were created after processing the nine images in Fig. 7 and superimposing all the spots. (a) All the spots are black on a white background. (b) The spots are colored according to the shift applied. The color code is for (i, j) given by ● (0,0), ● (0,1), ● (0,2), ● (1,0), ● (1,1), ● (1,2), ● (2,0), ● (2,1), and ● (2,2).

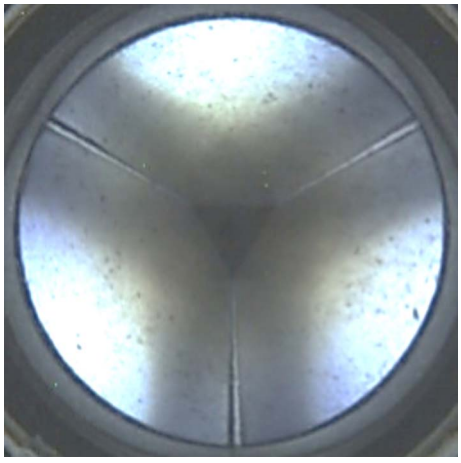

Fig. 9. Image of the three-LCD array displaying uniform illumination on each screen, but the reflected image has a nonuniform intensity.

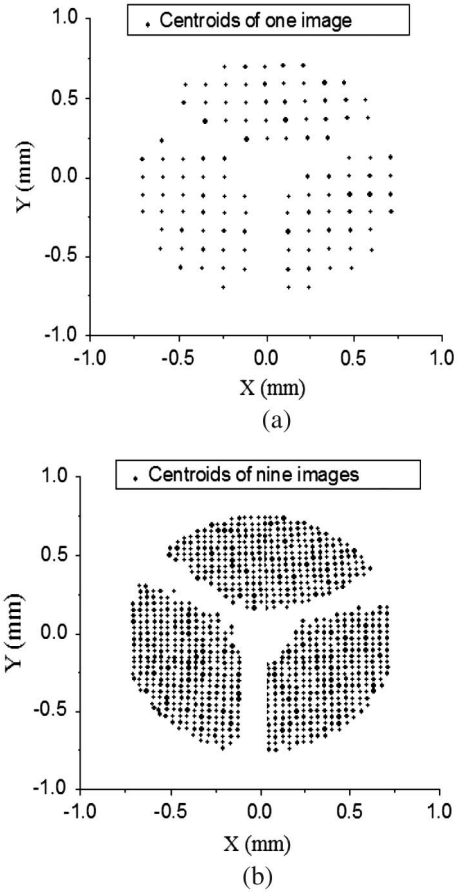

Fig. 10. (a) Plot of the positions of the spot centroids in Fig. 7(a). (b) Plot of the positions of the spot centroids for the nine images captured by using DyPoS (Fig. 7).

to spot number $t (i = 1, 2, 3, \ldots, N_t)$, and N_t is the total number of pixels within spot number t.

Figure 10(a) shows a plot of the positions of the 112 centroid spots obtained with only one image; the average spot separation is around 25 pixels. After applying the DyPoS method, the number of sampling points is increased as shown in Fig. 10(b); their density increases according to the number of shifts; a total of 961 centroids from all nine images are obtained, with their average separation reduced to approximately 8 pixels, that is, one-third of the original separation. Figure 10(b) also shows that after the shifting the distribution of spot centroids in the image plane is almost uniform for the three sectors.

Now the normals to the surface are evaluated from the actual incident and reflected rays $\hat{I}$ and $\hat{R}$, respectively, using

$$\hat{N} = \frac{\hat{R} - \hat{I}}{|\hat{R} - \hat{I}|}. \tag{19}$$

The incident ray is obtained using Eq. (1), with (x_1, y_1) the coordinates for each centroid. The reflected ray goes from the corresponding point of the null screen target to the point of incidence on the test surface; as this last point is unknown, it is approximated by the intersection point between the incident ray and the design surface. This approximation has proven to be adequate for evaluating surfaces [27,33]. In Fig. 11(a), the schematic idea for obtaining the normal components is shown;

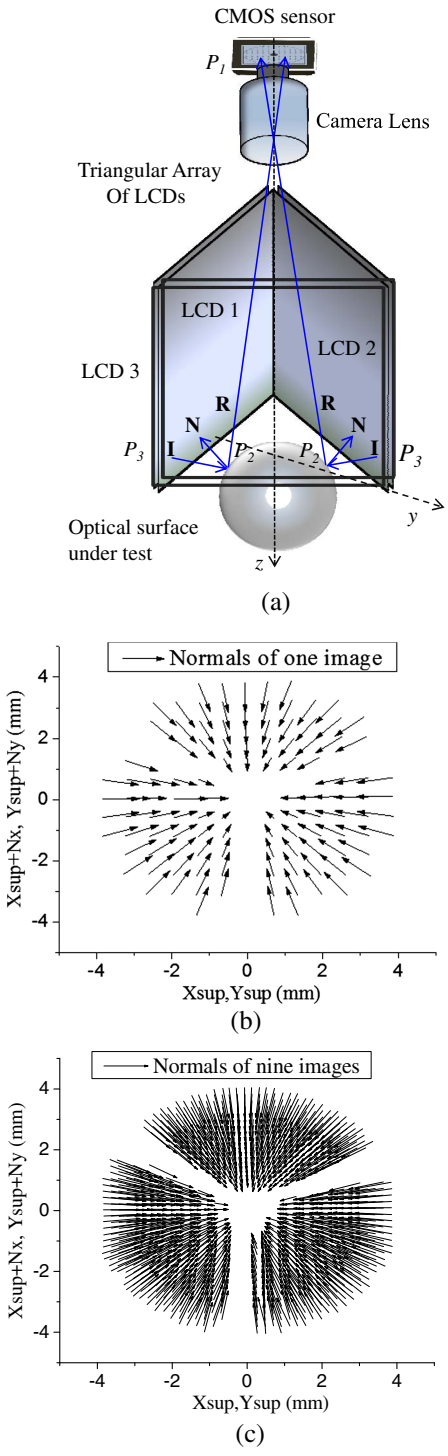

Fig. 11. (a) Layout of the test configuration. (b) Quotients of the normal components of one image. (c) Quotients of the normal components of nine images.

the resulting vector fields of the quotients $(N_x/N_z, N_y/N_z)$ of the normal components, for a single image and for all the nine images, are shown, correspondingly in Figs. 11(b) and 11(c). The fact that all these vectors are pointing to the origin of coordinates agrees with the symmetry of the measuring surface and indicates that it is well aligned.

The z coordinate for every sampling point on the surface is obtained by using the Shape of the Surface Equation originally proposed by Díaz-Uribe [34]:

$$z - z_1 = -\int_{C}^{(x,y)} \left(\frac{N_x}{N_z}\mathrm{d}x + \frac{N_y}{N_z}\mathrm{d}y\right), \tag{20}$$

where N_x, N_y, and N_z are the Cartesian components of the normal vector [Eq. (20)], and z_1 is the sagitta for one point on the surface; C is the path of integration, which starts on z_1. This expression is exact; evaluating the normals and performing the numerical integration are, however, approximate.

C. System Calibration

For calibrating the system, all geometrical parameters of the setup must be accurately measured. The image a and object b distances in Fig. 2 are determined by the principal points $(f_1, f_2, H_1, H_2, N_1, N_2)$ of the camera lens. All these parameters were measured by the method proposed in Ref. [35] and are listed in Table 3.

Also, the distortion and magnification of the camera lens were measured; by using a calibrated object composed of a square array of black dots on a white background, the real coordinates (x_o, y_o) of each object point are well known; by capturing an image of that array of points, the true coordinates (x_i, y_i) of their centroids can be computed. The relationship between object and image coordinates up to third degree when all aberrations, except distortion, are zero is given by

$$r_i = M_T r_o - E r_o^3, \tag{21}$$

where $r_i = \sqrt{x_1^2 + y_1^2}$ and $r_o = \sqrt{x_o^2 + y_o^2}$ are the image and object distances, respectively; M_T is the camera lens magnification and E is the distortion coefficient. To obtain the values of the last two coefficients, the r_i and r_o values for each dot in the object are measured. By fitting these data to Eq. (21), the next values were obtained, $M_T = 0.172 \pm 0.001$ and $E = (-6 \pm 8) \times 10^{-6}$ mm^{-2}. It is clear that the distortion seems to be negligible; but for a 15 mm field of view the centroid shift due to distortion is as large as 20 μm (5.6 pixels); the pixel size is 3.6 μm. Indeed, the measured area on the calibration sphere is only within a radius of 4 mm; the distortion shift is only 0.38 μm (1/10 of a pixel).

Other important parameters are the real dimensions of the LCD screens used as target; they are were measured with a Vernier, with 0.01 mm of accuracy. The values are in agreement with the technical data provided by the manufacturer and are listed at the beginning of Section 3.

Finally, a defocus error due to wrong positioning of the surface to be measured gives inaccurate results; this is an intrinsic problem in all corneal topographers. As shown clearly in Figs. 1 and 2, it is assumed that the reference system is centered in the vertex of the surface; we do not know, however, the exact position of the vertex of the surface under test. Essentially, the effect produced by the defocus is a change in image size, which gives a change in the spacing of the centroids, but also some additional distortion of the squared array. To avoid this, the surface was mounted on a precision linear stage, with movement parallel to the z axis; the surface was positioned in a place that was considered the correct one by looking for a better square array of spots on the image. Then the surface was moved to five

different positions along z axis, separated from the initial position −2, −1, 0, +1, and +2 mm; an image was captured in every step. For each image, the centroids of the spots were obtained and the x, y, and radial separations between adjacent spots were plotted versus the axial position z; the data were fit to linear functions to find the axial position where these separations are equal to the design value of 0.12 mm. This procedure gave a better positioning of the surface.

D. Numeric Integration

The numerical evaluation of the integral is performed using the trapezoidal rule for nonequally spaced data [3–5,27,30–33], given by

$$z_N = z_0 - \sum_{i=1}^{g-1}\left\{\left(\frac{N_{x_i}}{N_{z_i}} + \frac{N_{x_{i+1}}}{N_{z_{i+1}}}\right)\left(\frac{x_{i+1} - x_i}{2}\right) + \left(\frac{N_{y_i}}{N_{z_i}} + \frac{N_{y_{i+1}}}{N_{z_{i+1}}}\right)\left(\frac{y_{i+1} - y_i}{2}\right)\right\}, \quad (22)$$

where g is the number of points along some integration path; for a different path, the number of evaluation points can be different.

In Fig. 12(a), some of the 37 integration paths used for the integration with the set of points obtained from the original image without shift [Fig. 8(a)] are shown, whereas in Fig. 12(b), some selected integration paths used for the integrations with all the evaluation points are shown (a total of 132 paths were used in this case). For every case, the initial point P_o, where every integration path starts, is shown; the arrowheads represent the final point for each integration path.

In order to analyze the details of the evaluation, the data of the sagitta were fitted to a spherical surface [36], given by

$$z = z_0 + \frac{c[(x - x_0)^2 + (y - y_0)^2]}{1 + \{1 - c^2[(x - x_0)^2 + (y - y_0)^2]\}^{1/2}}, \quad (23)$$

where $c = 1/r$ is the curvature and (x_0, y_0, z_0) are the coordinates of the vertex of the surface; (x_0, y_0) are the decentering terms and z_0 is the defocus. The data fit was performed by using the Levenberg–Marquardt method [37].

E. Results

In Fig. 13(a), a 3D plot of the sagitta or elevation differences of the evaluated points with reference to the best sphere is shown, whereas in Fig. 13(b), a color map of the same differences is shown. In every plot in Fig. 13, the evaluated points are shown by black dots.

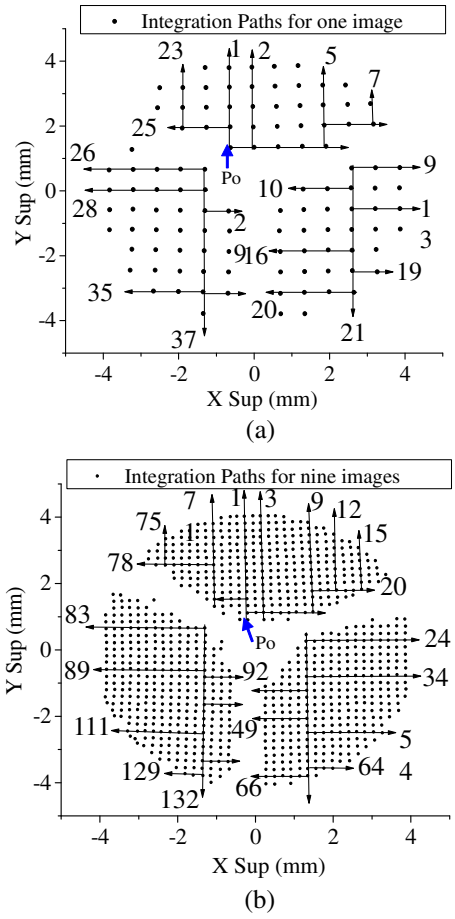

Fig. 12. (a) Integration paths for one image. (b) Integration paths for the total points with DyPoS.

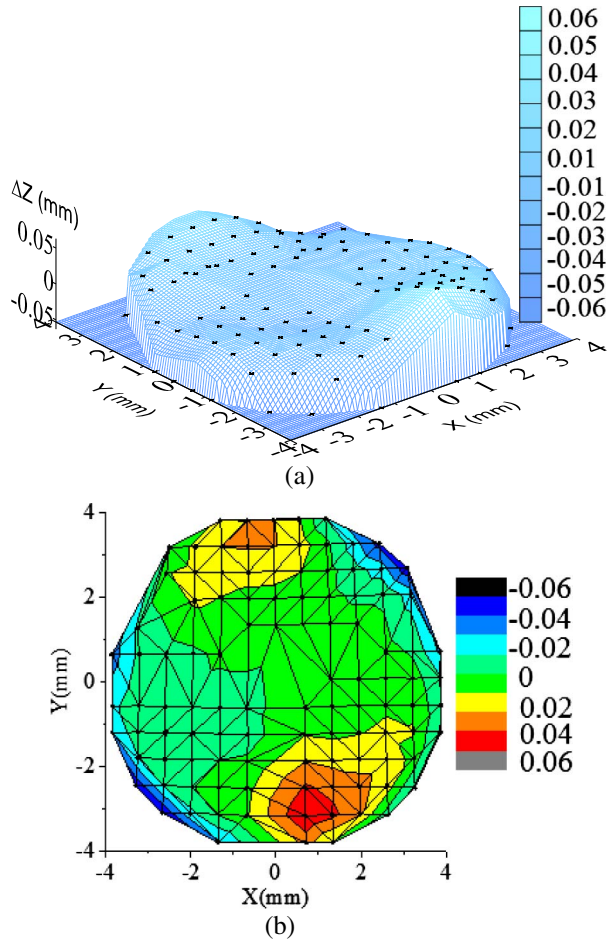

Fig. 13. (a) Plot of the differences in sagitta (z coordinate) between the evaluated surface and the best fit sphere for each of the 112 evaluation points on the measured surface without DyPoS. (b) Map of sagitta differences or elevation on each evaluation point.

Table 4. Measured Parameters of the Best Fit Conic Surface with and without DyPoS ($r = 6.37$ mm, $P = 52.98$) (the Differences from Nominal Values are within Parentheses)

Calibration Spherical Surface	Radius Obtained (mm)	Dioptric Power ($D = m^{-1}$)	P–V Sagitta Differences (mm)	RMS Sagitta Differences (mm)
Without (DyPoS)	5.89 (0.48)	57.30 (4.32)	0.08	0.0228
With (DyPoS)	6.17 (0.20)	54.70 (1.72)	0.04	0.0152
Differences (no DyPoS–DyPoS)	−0.28	2.6	0.04	0.0076 (33%)

In this case, the P–V difference in sagitta between the evaluated points and the best fit is $\delta z_{pv} = 80$ μm and their RMS value is $\delta z_{\mathrm{RMS}} = 0.023$ mm. The numerical values for the parameters obtained with the fit are shown in the second row of Table 4. There we notice that the radius of curvature differs by approximately 0.58 mm or about 9% of the real value.

The results obtained with the DyPoS method are as follows: the number of spots is increased almost nine times, thus reducing the average separation three times; as a consequence, the accuracy is improved in sagitta, but also the spatial frequencies of the surface deformations are increased three times along the x and y directions [see Fig. 14(a)]. In the third row of Table 4 it is shown that the P–V and RMS values for the sagitta differences are smaller when DyPoS is applied; here $\delta z_{pv} = 40$ μm and $\delta z_{\mathrm{RMS}} = 0.0152$ mm, thus the error is reduced by 33%, in comparison with the no DyPoS results; furthermore, the radius of curvature value is improved because the difference from the real value is approximately 0.20 mm or only 3% of the real value.

It is worth stating here that the reference sphere used for the experiments in this section was measured with a micrometric screw; these data show that the surface has spherical departures below 2 μm. Then the P–V and RMS values of the differences in sagitta reported in Table 4 are estimators of the total error obtained with the method reported here, including alignment and numerical systematic and random errors. In particular, for the radius of curvature and power measurement, the differences are small as compared with the nominal values; they are large, however, if we assume these differences as the uncertainty of the measurement. Currently the accuracy required for clinical corneal topography must be around 1/8 D. So the uncertainty must be reduced to at least one-tenth of the present value. These results do not represent a fundamental limit; they can be improved with better alignment of the three LCDs of the surface or by improving the numerical routines.

4. ADDITIONAL COMMENTS

The above results are, to the best of our knowledge, a first demonstration of the capabilities of using this LCD array as a target for measuring a reflecting convex spherical surface of similar

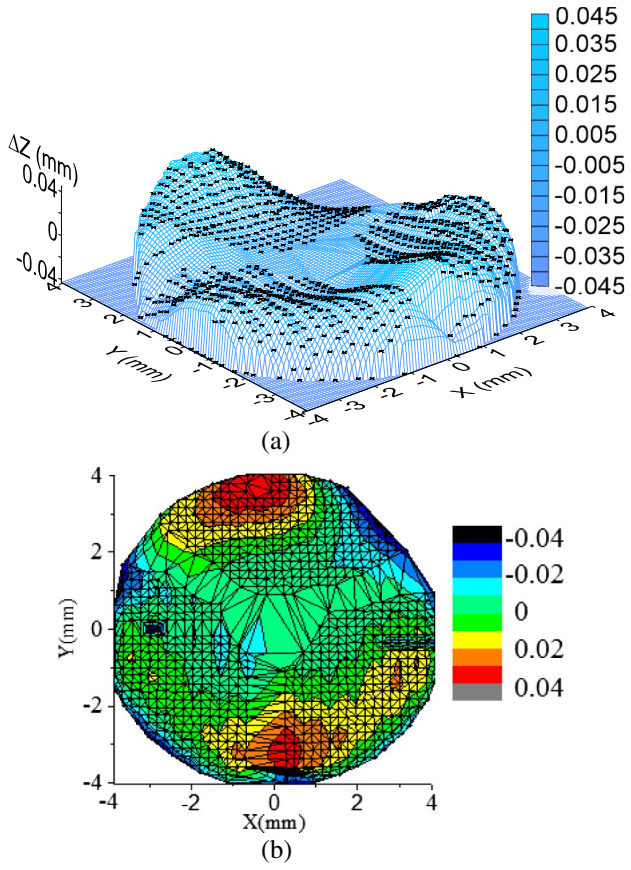

Fig. 14. Quantitative results obtained with nine shifts by DyPoS. (a) Differences in sagitta between the measured surface and the best-fitting spherical surface. (b) Map of sagitta differences or elevation on each evaluation point.

dimensions to the human corneal surface, including the accuracy with and without DyPoS; this is a common practice in corneal topography research and, according to Ref. [38], the evaluation of a calibration surface gives information about the accuracy of the device and method. A first image of the human cornea with the triangular prism arrangement of LCDs is shown in Fig. 15. It can be observed that a square array of color dots covers the total area of the corneal surface. Even though the method and device have still not been proved quantitatively on a real cornea, the null screen method has been extensively demonstrated for measuring the deformations of many different optical surfaces, which include concave and convex conics of different sizes [3–5,27,33] and even surfaces without symmetry of revolution, such as off-axis [30,31] and highly astigmatic paraboloids [39]. In addition, the LCD arrangement proposed here gives a nearly flat image adequate for the usual optical systems used with image sensors [8].

The additional capability of LCDs as a target in a corneal topographer is the ability to display different target geometries without changing the proposed DPF configuration or the relative positions of the target and the test surface; i.e., we can have different geometric patterns observed in the image plane, such as square or radial arrays of lines or dots [see Figs. 16(a)–16(c)].

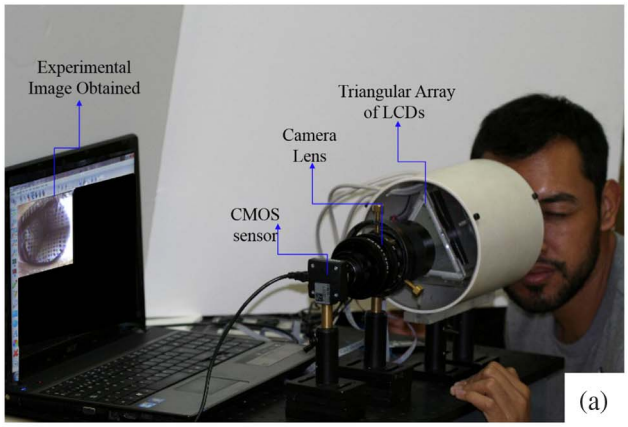

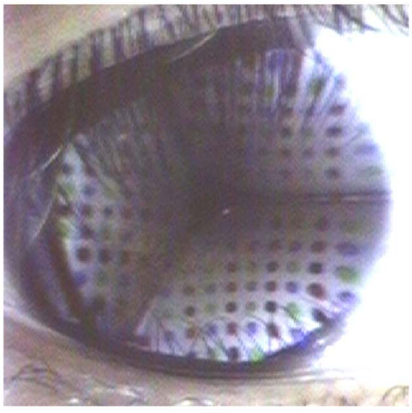

Fig. 15. (a) Triangular array of LCDs testing a human eye. (b) Square array of color dots on a real cornea.

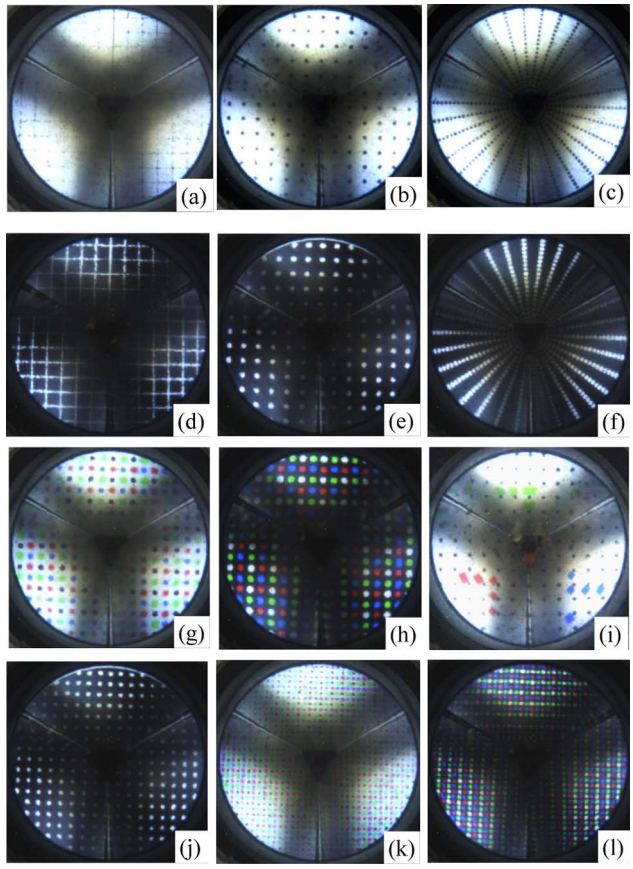

Fig. 16. Different target geometries displayed with the configuration of LCDs. (a)–(c) Square and radial arrangements of dots on a white background. (d)–(f) Square and radial arrangements of dots on a black background. (g)–(i) Color spots on a white and black background. (j)–(l) Different number of dots in the pattern.

Furthermore, it is possible to revert the contrast of the null screen [Figs. 16(d)–16(f)], or even design chromatic null screens to ease the identification of the different spots [Figs. 16(g)–16(i)]; also, it is possible to deploy different numbers of dots in the pattern [Figs. 16(j)–16(l)].

In Fig. 16(i), we show a set of strategic color marks in the null screen target. In this case, the colors were used in order to simplify the correspondence during the quantitative evaluation between image centroids and target dots, even if a few spots are missing [25,26].

One drawback of the use of LCDs as targets, however, is the illumination provided by the set of LCDs on the image, it is not homogenous; i.e., the experimental patterns of dots in Figs. 7, 15, and 16 have areas with low intensity. This problem makes it difficult to separate the spots and obtain their centroids for the quantitative evaluation in the numerical integration procedure used [34]. This problem requires the development of subroutines for processing experimental images with nonuniform contrast. In Fig. 9, the image of uniformly illuminated LCD screens is shown; this image is useful for the compensation of the variable contrast of the target image.

It is well worth stating here that the illumination provided by the LCD array is fairly harmless to the human eye. There are some good reasons that support this claim: first of all, these devices are intended for direct observation with the naked eye; the manufacturer claims in the Legal Notices of the User Manual [40] that it complies with the applicable safety FCC standards, the US DHHS safety performance, and FDA Radiation Performance Standards 21 CFR Subchapter J. Second, the light power measured at the eye plane is 12 μW and the power density is 16.6 $\mu W \cdot cm^2$; very small indeed, this is 1.2% of the maximum power of a laser beam class 2, which is 1 mW. Third, each LCD screen acts as an extended light source, all three covering a solid angle of around 1.9π steradians; the smaller angle subtended by a point of one LCD is around 9.6° from the z axis. Finally, the illumination arriving at the eye position is diffuse, so it does not have a defined preferred direction; the light arriving at the retina is never focused on a small region, so the power density does not become so large that it can produce some damage. According to Sliney and Freasier [41], the maximum permissible exposition for continuous sources is around 100 $mW \cdot cm^2$, so the array of LCDs used in this paper is clearly safe for the human eye.

5. CONCLUSIONS

In this paper, a triangular prism LCD arrangement to display null screens for applying DyPoS as a target for an experimental corneal topographer has been proposed. This is aimed at the

measurement of corneal topography and experimental results obtained for one calibration sphere have been presented. It has been shown that when we apply the DyPoS method the evaluation of the surface is improved for both sagitta and lateral resolution. In the example with DyPoS with a total of nine images with the spots shifted, the radius of curvature becomes closer to the real value: from a 9% difference for only one image to 3% for the nine images; on the other hand, the RMS difference in sagitta improved from 0.0228 μm for one image to 0.0152 μm for the nine images. In addition, it was demonstrated that the device can scan the surface with a denser sampling, thus reducing the average separation of the evaluation points. We can conclude that by increasing the number of points, the resolution and accuracy are also increased.

Funding. Universidad Nacional Autónoma de México, DGAPA-PAPIIT (IN114110-2, IT101414, IT101912); Consejo Nacional de Ciencia y Tecnología (CONACyT).

Acknowledgment. The authors thank Juan Ricardo Damian Zamacona for useful support in adjusting the electronics setup and Neil Bruce for help to review the manuscript.

REFERENCES

1. R. Díaz-Uribe and M. Campos-García, "Null-screen testing of fast convex aspheric surfaces," Appl. Opt. **39**, 2670–2677 (2000).
2. R. Díaz-Uribe, R. Bolado-Gomez, M. Campos-García, and M. Avendaño-Alejo, "Medium precision optical testing of a fast concave elliptical mirror by a cylindrical null screen," Proc. SPIE **6034**, 60340Y (2006).
3. V. I. Moreno-Oliva, M. Campos-García, R. Bolado-Gómez, and R. Díaz-Uribe, "Point shifting in the optical testing of fast aspheric concave surfaces by a cylindrical screen," Appl. Opt. **47**, 644–651 (2008).
4. V. I. Moreno-Oliva, M. Campos-García, and R. Díaz-Uribe, "Improving the quantitative testing of fast aspherics with two-dimensional point shifting by only rotating a cylindrical null screen," J. Opt. A **10**, 104029 (2008).
5. M. Campos-García, R. Bolado-Gómez, and R. Díaz-Uribe, "Testing fast aspheric concave surfaces with a cylindrical null screen," Appl. Opt. **47**, 849–859 (2008).
6. E. Ghozeil, "Hartmann and other screen tests," in *Optical Shop Testing*, D. Malacara, ed., 2nd ed. (Wiley, 1992), pp. 367–396.
7. D. D. McCracken and W. S. Dorn, *Numerical Methods and FORTRAN Programming* (Wiley, 1964), pp. 178–183, Chap. 6.
8. Y. Mejía-Barbosa and D. Malacara-Hernandez, "Object surface for applying a modified Hartmann test to measure corneal topography," Appl. Opt. **40**, 5778–5786 (2001).
9. S. A. Klein, "Axial curvature and the skew ray error in corneal topography," Optom. Vis. Sci. **74**, 931–994 (1997).
10. S. A. Klein, "Corneal topography reconstruction algorithm that avoids the skew ray ambiguity and the skew error," Optom. Vis. Sci. **74**, 945–962 (1997).
11. N. K. Tripoli, K. L. Cohen, P. Obla, J. M. Coggins, and D. E. Holmgren, "Height measurement of astigmatic test surfaces by a keratoscope that uses plane geometry surface reconstruction," Am. J. Ophthalmol. **121**, 668–676 (1996).
12. J. Schwiegerling and J. M. Miller, "A videokeratoscope using a distorted checkerboard target," in *Oral presentation at the Vision Science and its Applications (OSA) Annual Meeting*, Santa Fe, New Mexico, 1998.
13. S. A. Klein, "Uniqueness of corneal shape from Placido ring images," in *Vision Sciences and its Applications*, OSA Technical Digest Series (Optical Society of America, 1996), Vol. **1**, pp. 204–207.
14. R. Rand, R. A. Applegate, and H. C. Howland, "A mathematical model of Placido disk keratometer and its implication for recovery of corneal topography," in *Vision Sciences and its Applications*, OSA Technical Digest Series (Optical Society of America, 1997), Vol. **1**, pp. 46–49.
15. J. Joris Snellenburg, B. Braaf, E. A. Hermans, G. L. R. van der Heijde, and V. A. Sicam, "Forward ray tracing for image projection prediction and surface reconstruction in the evaluation of corneal topography systems," Opt. Express **18**, 19324–19338 (2010).
16. F. M. Vos, R. G. L. van der Heijde, H. J. W. Spoelder, I. H. M. van Stokkum, and F. C. A. Groen, "A new instrument to measure the shape of the cornea based on pseudorandom color coding," IEEE Trans. Instrum. Meas. **46**, 794–797 (1997).
17. T. Swartz, L. Marten, and M. Wang, "Measuring the cornea: the latest developments in corneal topography," Curr. Opin. Ophthalmol. **18**, 325–333 (2007).
18. J. H. Massig, E. Lingelbach, and B. Lingelbach, "Videokeratoscope for accurate and detailed measurement of the cornea surface," Appl. Opt. **44**, 2281–2287 (2005).
19. M. A. Halstead, B. A. Barsky, S. A. Klein, and R. B. Mandell, "A spline surface algorithm for reconstruction of corneal topography from a videokeratographic reflection pattern," Optom. Vis. Sci. **72**, 821–827 (1995).
20. V. A. Sicam, J. Coppens, T. J. van den Berg, and R. G. van der Heijde, "Corneal surface reconstruction algorithm that uses Zernike polynomial representation," J. Opt. Soc. Am. A **21**, 1300–1306 (2004).
21. J. Turuwhenua, "Corneal surface reconstruction algorithm using Zernike polynomial representation: improvements," J. Opt. Soc. Am. A **24**, 1551–1561 (2007).
22. A. Estrada-Molina, "Topografo Corneal Portatil Basado en Pantallas Nulas (Portable corneal topographer based on null screens)," Ph.D. dissertation (Universidad Nacional Autonoma de Mexico, 2014).
23. Z. Fazekas, A. Soumelidis, A. Bódis-Szomorú, and F. Schipp, "Specular surface reconstruction for multi-camera corneal topographer arrangements," in *Proceedings of IEEE EMBS Conference*, Canada, August 24–28, 2008, pp. 2254–2257.
24. A. Victor, H. de Vries, M. Huijbregtse, and M. Michiel, "Image processing of irregular corneas in color-coded multiple-point-source corneal topography (CMCT)," Investig. Ophthalmol. Vis. Sci. **52**, 4189 (2011).
25. J. Beltrán-Madrigal and R. Díaz-Uribe, "Progress in the design of chromatic null screens to test cylindrical parabolic concentrators," Proc. SPIE **8011**, 80111R (2011).
26. M. I. Rodríguez-Rodríguez, A. Jaramillo-Núñez, and R. Díaz-Uribe, "New design of null screens to simplify the correspondence during the quantitative evaluation of optical surfaces," Proc. SPIE **8838**, 883810 (2013).
27. V. I. Moreno-Oliva, M. Campos-García, F. S. Granados-Agustín, A. Santiago-Alvarado, and R. Díaz-Uribe, "Improving fast aspheric convex surface test with dynamic null screens using LCDs," Appl. Opt. **50**, 3101–3109 (2011).
28. M. I. Rodríguez-Rodríguez, A. Jaramillo-Núñez, and R. Díaz-Uribe, "Dynamic point shifting in null screen videokeratometry," Proc. SPIE **8011**, 80119H (2011).
29. J. Heikkila, "Geometric camera calibration using circular control points," IEEE Trans. Pattern Anal. Mach. Intell. **22**, 1066–1077 (2000).
30. M. Avendaño-Alejo and R. Díaz-Uribe, "Testing a fast off-axis parabolic mirror using tilted null-screens," Appl. Opt. **45**, 2607–2614 (2006).
31. M. Avendaño-Alejo, V. I. Moreno-Oliva, M. Campos-García, and R. Díaz-Uribe, "Quantitative evaluation of an off-axis parabolic mirror by using a tilted null-screen," Appl. Opt. **48**, 1008–1015 (2009).
32. M. Campos-Garcia, C. Cossio-Guerrero, V. I. Moreno-Oliva, and O. Huerta-Carranza, "Surface shape evaluation with a corneal topographer based on a conical null-screen with a novel radial point distribution," Appl. Opt. **54**, 5411–5419 (2015).
33. M. Campos-García, R. Díaz-Uribe, and F. S. Granados-Agustin, "Testing fast aspheric convex surfaces with a linear array of sources," Appl. Opt. **43**, 6255–6264 (2004).
34. R. Díaz-Uribe, "Medium precision null screen testing of off-axis parabolic mirrors for segmented primary telescope optics: the Large Millimeter Telescope," Appl. Opt. **39**, 2790–2804 (2000).

35. Y. Mejia, "Improvement in the measurement of focal length using spot patterns and spherical aberration," Appl. Opt. **52**, 5577–5584 (2013).
36. D. Malacara, "Mathematical representation of an optical surface and its characteristics," in *Optical Shop Testing* D. Malacara, ed., 3rd ed. (Wiley, 2007), pp. 832–836.
37. P. R. Bevington and D. K. Robinson, *Data Reduction and Error Analysis for the Physical Sciences*, 2nd ed. (McGraw-Hill, 1992), pp. 161–166.
38. A. Estrada-Molina and R. Díaz-Uribe, "Accuracy test for a corneal topographer based on null-screen method: preliminary results," in *Latin America Optics and Photonics Conference* (Optical Society of America, 2014), paper LTh4A.45.
39. V. I. Moreno-Oliva, R. Díaz-Uribe, and M. Campos-Garcia, *Shape Measurement of Solar Collectors by Null Screens*, R. M. Ochieng, ed. (Sciyo, 2010), pp. 169–186, Chap. 8.
40. "DYNEX 7" digital picture frame DX-DPF7 user guide" (USA, 2007), http://www.dynexproducts.com/.
41. D. H. Sliney and B. C. Freasier, "Evaluation of optical radiation hazards," Appl. Opt. **12**, 1–24 (1973).